Comparisons of bpy and phen Ligand Backbones in Cr-Mediated

(Co-)Electrocatalytic CO₂ Reduction

Amelia G. Reid, Megan E. Moberg, Connor A. Koellner, Juan J. Moreno, Shelby L. Hooe, Kira R. Baugh, Diane A. Dickie, and Charles W. Machan*

* - machan@virginia.edu; ORCID 0000-0002-5182-1138

AGR ORCID 0000-0002-2868-4091; MEM ORCID 0000-0003-2083-9877; CAK ORCID 0000-0001-5395-9141; SLH ORCID 0000-0002-6991-2273; JJM ORCID 0000-0003-1809-6170; DAD ORCID 0000-0003-0939-3309

Department of Chemistry, University of Virginia, PO Box 400319, Charlottesville, VA 22904-4319

Abstract:

Due to the rise in atmospheric carbon dioxide (CO₂) concentrations, there is a need for the development of new strategies to enhance the selectivity and activity of the electrocatalytic conversion of CO₂ to value-added products. The incorporation of redox mediators (RMs) as cocatalysts to enhance the transfer of redox equivalents during catalysis has been gaining more attention in recent years across a variety of small molecule transformations. We have shown that using Cr-centered complexes with sulfone-based RMs leads to an enhancement of CO2 reduction electrocatalysis under protic conditions via an inner-sphere mechanism. In these co-catalytic systems, an oxygen atom of the reduced RM binds to the Cr center to form a key intermediate stabilized by pancake bonding between the reduced aromatic components of the catalyst ligand backbone and the RM. This interaction facilitates the transfer of an electron and accesses a more kinetically favorable reaction pathway. Here, we show that expanding the aromatic character of the ligand backbone of the catalyst as well as the RM can cause a greater enhancement of coelectrocatalytic activity. These results suggest that further activity improvements can be achieved by focusing on the kinetic and thermodynamic parameters which control association between the catalyst and RM.

Introduction:

Since the industrial revolution, the amount of accumulated carbon dioxide (CO₂) pollution in the atmosphere has been estimated to be 1.5 trillion tons, and this increase is the leading contributor to the current global climate crisis. Electrocatalytic reduction of CO₂ to value-added chemical products could be used to both reduce current emissions and atmospheric concentrations. If earth-abundant transition metals and renewable energy sources, like wind or solar, are used to drive the electrochemical reduction of CO₂ to carbon monoxide (CO), the production of chemical feedstocks and fuels could be decoupled from petrochemical sources and feasibly scaled. While earth-abundant transition metal complexes have been studied across a range of metal centers for the reduction of CO₂, the use of chromium (Cr)-centered homogeneous catalysts remains relatively underdeveloped with, to our knowledge, only three known catalysts reported by our group being active for the reduction of CO₂ to CO.⁷⁻⁹

There is growing interest in the use of redox mediators (RMs) to improve catalytic small molecule conversion processes. ¹⁰ Previous examples of using RMs have increased the activity of the catalytic system and/or shifted reaction selectivity by facilitating electron transfer, avoiding high energy intermediates, or avoiding competitive pathways. ⁹⁻²³ While these examples are inspired by relatively static biological systems, such as the electron transport chain ²⁴ and iron-sulfur clusters, ²⁵⁻²⁷ RMs are free to interact directly with molecular active sites, enabling the use of molecular design principles to consider kinetic aspects of the catalyst and mediator interaction, in addition to considering the thermodynamic positioning of redox processes in a manner analogous to the biological systems. ²⁸ When the transfer of electrons from RMs to an active site is linked to a proton transfer event, these co-catalysts have been referred to as electron-proton transfer mediators (EPTMs). ^{13, 14} To our knowledge, only two examples of CO₂ reduction with a RM that can be regenerated by the electrode have been reported outside of our group. ^{20, 21} The system

reported by Smith *et al.* relies on a NADH-inspired EPTM that works to enhance the transfer of an electron and proton to an iron porphyrin catalyst in order to increase the activity of the system.²⁰ More recently, Dey *et al.* demonstrated the selectivity of the classic Mn(bpy)(CO)₃Cl catalyst can be shifted from CO to formic acid by using an iron-sulfur cluster EPTM which promotes the formation of a M–H species at modest reducing potentials.²¹

Both of these previous reports rely on proton-coupled electron transfer reaction steps, where hydrogen atom equivalents are delivered to the metal center or metal-bound substrate. Our group has reported a series of systems with sulfone-containing RMs and Cr-centered catalysts that increase the rate of catalysis through an inner-sphere electron transfer mechanism *sensu stricto*, where the RM coordinates to the catalyst active site and transfers an electron equivalent to the metal center directly. In a recent study, we proposed that this co-catalyst assembly is stabilized by pancake bonding (PB) between the RM and bipyridine (bpy) ligand backbone under protic conditions. A PB interaction occurs when highly delocalized π -radicals in aromatic systems are positioned within short distances of one another such that vertical atom overlap can occur, creating a pathway for electron transfer. We observed that as the reduction potential of our catalyst and RM are shifted closer to each other, the resulting PB is more favorable (Figure 1). Since all catalyst-RM adducts were found to have comparable calculated barriers for the proposed rate-determining step, it is the favorability of their association which dictates the observed activity.

However, these studies also showed the effects of the steric profile of the catalyst in the case where *tert*-butyl groups were appended to the 4,4′ positions of the bipyridine-based ligand backbone. When the DBTD RM was modified at the 2,8 positions to tune its reduction potential and aromatic character, steric clash with these *tert*-butyl groups was introduced, resulting in a decrease of vertical atom-atom overlap (**Figure 1**). Consequently, energetically well-matched

molecular orbitals were kinetically prevented from forming optimal interactions, lowering the quality of the PB interaction. Therefore, we were interested in exploring alternative catalyst ligand structures to address this limitation and explore how it was balanced with dispersion interactions. Our hypothesis was that increased aromatic character in the ligand backbone could better isolate the role of PB strength in co-electrocatalytic activity from other stereochemical forces.

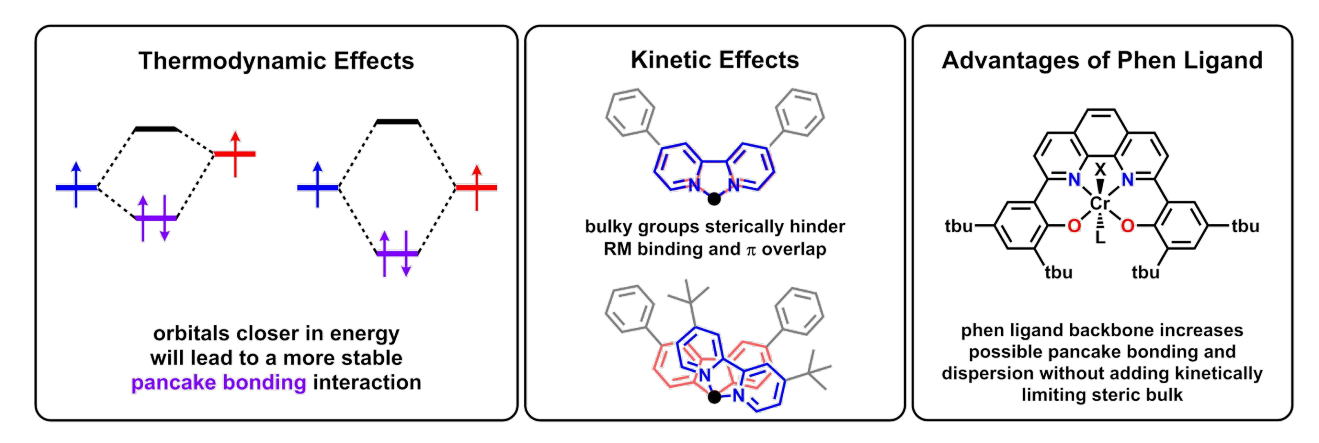


Figure 1. Overview of thermodynamic and kinetic effects which play a role in pancake bonding between Cr catalyst and sulfone RM and the advantages of the new phen ligand framework presented in this work. The two other components which also contribute to the association of the catalyst and RM are dispersion interactions and Cr–O bond formation; X = Cl, $L = H_2O$ or DMF.

Here, we report a new catalyst for the reduction of CO₂ to CO with a phenanthroline-based backbone inspired by our previous ligand frameworks. Additionally, we analyze this catalyst with two sulfone-based RMs and compare the trends in activity against our previously reported Cr catalysts with bipyridine- and *tert*-butyl-substituted bipyridine backbones.⁹ This new phenanthroline-based catalyst demonstrates that by considering the thermodynamic and kinetic aspects of pancake bond formation (vertical atom-atom overlap and steric hinderance) between the Cr complex and RM, significant enhancements in co-electrocatalytic rate can be achieved. Interestingly, we find there to be a compensatory relationship with the other contributors to the formation of the co-catalytic assembly: Cr-sulfone bond formation and dispersion interactions.

Results:

Electrochemistry of Cr Catalysts

The synthesis of the (tbudhphen)(H)₂) ligand (**Figure S2**) was carried out as previously reported.³⁰ The comparable metalation of the (tbudhphen(H)₂) ligand to make Cr(tbudhphen)Cl(H₂O) (**2**) used a modified literature procedure (see Supporting Information (SI)) and **2** was characterized by UV-vis (**Figure S3**), NMR (**Table S2**), electrospray ionization-mass spectrometry (ESI-MS) (**SI**), microanalysis (**SI**), and single-crystal X-ray diffraction (XRD) studies (**Figure 2**).

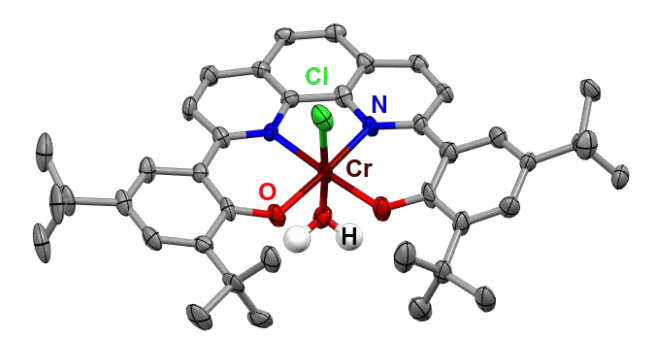


Figure 2. Molecular structure of $Cr(^{tbu}dhphen)Cl(H_2O)$ (2) obtained from single-crystal X-ray diffraction studies. Blue = N, red = O, gray = C, green = Cl, maroon = Cr, white = H atoms of bound water molecule; thermal ellipsoids at 50%; ligand H atoms and solvent molecules omitted for clarity; only one of two chemically equivalent by crystallographically distinct molecules in the asymmetric unit is shown. CCDC 2221536.

Cyclic voltammetry (CV) experiments were performed on **2** in *N*,*N*-dimethylformamide (DMF) with 0.1 M tetrabutylammonium hexafluorophosphate (TBAPF₆) as the supporting electrolyte like was done previously for $Cr(^{tbu}dhbpy)Cl(H_2O)$ (**1**) (structures shown in **Figure 3**). Under argon (Ar) saturation conditions, both catalysts exhibit three redox features and those for **2** ($E_p = -1.67$ and -1.79 V and $E_{1/2} = -1.96$ V versus ferrocenium/ferrocene (Fc⁺/Fc), **Figure 4**) are approximately 10 mV more negative than those for **1** ($E_p = -1.66$ and -1.78 and $E_{1/2} = -1.95$ V vs. Fc⁺/Fc). Due to the similarity in redox potentials, as well as the observed reversibility and relative current densities of these waves, we propose similar assignments to those previously reported for

1.^{7,9,31} For complex **2**, the first two redox features are chemically related and coalesce at scan rates ≥2000 mV/s, consistent with their assignment to the end-states of a solvent displacement equilibrium involving the axial chloride ligand (**Figure S4** and **S5**). Overall, these two chemically related features correspond to a single-electron reduction of the starting complex **2**. Similar to complex **1**, the third feature observed for **2** at $E_{1/2} = -1.96$ V vs. Fc⁺/Fc represents the formal addition of a second electron overall. The addition of PhOH under Ar saturation leads to only a slight change in the observed redox features (**Figure 4A**, green), indicating a lack of intrinsic activity for hydride formation or hydrogen evolution. ³²⁻³⁴ Additionally, the redox features for **2** remain unchanged under CO₂ saturation in the absence of added proton donor (**Figure 4A**, red), demonstrating the absence of aprotic CO₂ reduction activity. The electrochemistry of the Cr(tbudhtbubpy)Cl(H₂O) (**3**) catalyst is very similar to that of **1** and **2**. However, due to the electron donating character of the *tert*-butyl groups substituted on the bpy backbone, all of the redox events are shifted to more negative potentials. ⁹

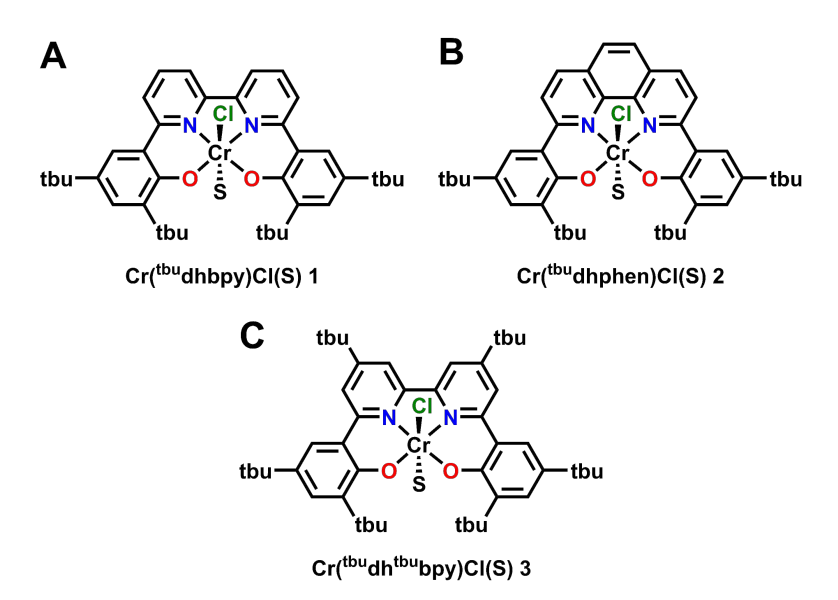


Figure 3. Structures of Cr catalysts discussed in this paper where S is either a H₂O or DMF solvent molecule.

The addition of 0.6 M PhOH under CO₂ saturation conditions leads to a large increase in current density and loss of reversibility at the third redox feature ($E_{cat/2} = -1.96 \text{ V}$ vs. Fc⁺/Fc), consistent with the electrocatalytic reduction of CO₂ (Figure 4A). Notably, there is not a significant difference between this increase in current density for 2 and that observed for 1 under otherwise identical conditions (Figure 4B). We attribute this similarity in part to minimal difference in catalyst standard reduction potential ($E_{1/2} = -1.95 \text{ V}$ for 1; $E_{1/2} = -1.96 \text{ V}$ for 2 vs Fc⁺/Fc). Complex 3 exhibits catalytic activity at a more negative standard reduction potential of $E_{1/2} = -2.00 \text{ V}$ vs Fc+/Fc, reflecting the contributions of the electron-donating tert-butyl groups. The catalytic activity of complexes 1 and 3 were previously found to have a first-order concentration dependences with respect to catalyst, PhOH, and CO₂.^{7, 9} Comparable electroanalytical CV experiments with variable concentrations of 2, PhOH, and CO₂ revealed that the rate of catalysis is likewise first-order with respect to all three components (Figures S6-S8). Interestingly, the saturation of catalytic current with respect to [PhOH] occurred at 0.6 M for 2, while the response saturated at 0.45 M for 1.7 Saturation of catalytic current density for complex 3 occurred at [PhOH] of 0.40 M.9

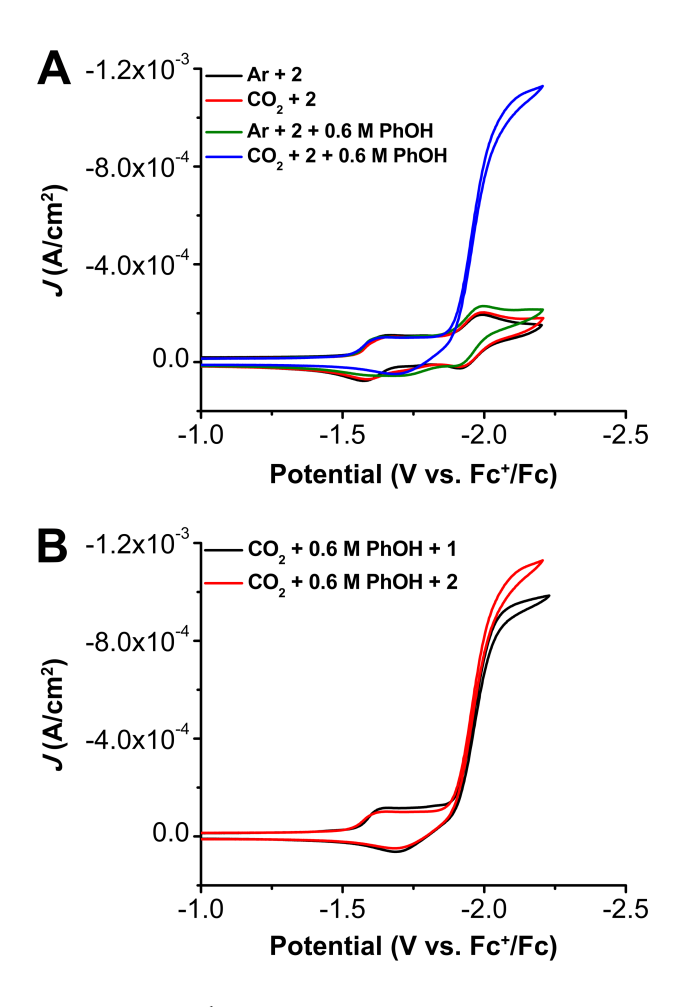


Figure 4. (A) Comparison CVs of Cr(^{tbu}dhphen)Cl(H₂O) **2** under Ar and CO₂ saturation conditions with and without 0.6 M PhOH. (**B**) Comparison CVs of Cr(^{tbu}dhbpy)Cl(H₂O) **1** and Cr(^{tbu}dhphen)Cl(H₂O) **2** under CO₂ saturation with 0.6 M PhOH. Conditions: 1.0 mM catalyst, 0.1 M TBAPF₆/DMF; glassy carbon working electrode, glassy carbon rod counter electrode, Ag/AgCl pseudoreference electrode; referenced to Fc⁺/Fc internal standard; 100 mV/s scan rate.

To compare the activity and selectivity of **1** and **2**, controlled potential electrolysis (CPE) was performed at an applied potential of –2.3 V vs Fc⁺/Fc under CO₂ saturation with added PhOH, with analysis of gaseous product formation by gas chromatography (GC). Initially, 0.6 M added PhOH was used with **2** to compare the activity and selectivity of the two catalysts, based on previously reported results for **1**.^{7, 11, 12} Under these conditions, **2** is selective for the reduction of CO₂ to CO with a Faradaic efficiency (FE_{CO}) of 94±11% over 4.6 turnovers (**Figure S9** and **Table S3**). Note that turnovers have been calculated to show the catalytic nature of the process and do

not represent a measurement to the full loss of activity. Based on the observed current density in the CPE experiment, the turnover frequency (TOF_{CPE}) was estimated to be 4.57 s⁻¹ with 0.6 M PhOH. Since **2** was shown to have a higher PhOH saturation (**Figure S7**) than **1** in initial CV studies,⁷ we performed a second CPE experiment under the same conditions, but with 1.0 M PhOH as the proton source (**Figure S10** and **Table S4**). The results of this experiment showed no change in product selectivity (FE_{CO} = $101\pm3\%$, **Table 1**) and only a minor increase in activity with a TOF_{CPE} of 4.90 s⁻¹. The electrode from this experiment was rinsed and the CPE experiment was repeated under analogous conditions in the absence of **2**, where the formation of a non-quantifiable amount of CO and significant H₂ was observed (**Figure S11** and **Table S5**). These results are in good agreement with our previously reported PhOH control CPE experiments and are consistent with a homogeneous catalytic process. ^{11, 12} The TOF_{CPE} values obtained for both **1** and **2** are lower than that observed for catalyst **3**, 9.29 s⁻¹, which also showed selective Faradaic efficiency for CO (FE_{CO} = $95\pm8\%$, **Table 1**). ⁹

Co-Electrocatalysis Under Protic Conditions

We have previously established that the combination of Cr complexes with a bpy-based ligand backbone and aromatic sulfone-based RMs results in a co-electrocatalytic system and increased activity for the reduction of CO_2 under protic conditions.^{9, 11, 12} For comparison with the phen-based system reported here, we compared the trends in activity when dibenzothiophene-5,5-dioxide (DBTD) and 2,8-diphenyldibenzothiophene-5,5-dioxide (Ph₂DBTD) are used as the RM (**Figure 5A**).^{9, 11, 12} Since the standard reduction potential of both RMs is more negative than that of the catalyst, the reduction potential of the mediator controls the co-electrocatalytic operating potential.^{9, 11, 12} DBTD and Ph₂DBTD have $E_{1/2}$ values of -2.25 V and -2.12 V vs Fc⁺/Fc, respectively (**Figure S12**). Notably, previous studies comparing co-catalytic systems with these

RMs have demonstrated inverse potential scaling with respect to activity: Ph₂DBTD showed the highest catalytic activity at the lowest overpotential with complex 3.9 Figure 5 shows that the inclusion of both RMs results in an increase in the observed CV current density for complex 2 as well, however, the relative increase upon RM inclusion is different between 1 and 2. The co-catalytic systems with 1 as the catalyst demonstrate more of an increase in current density when DBTD is the RM compared to the system with Ph₂DBTD (Figure 5B). For complex 2, the opposite trend is observed, with Ph₂DBTD as the RM there is a larger increase in current density (Figure 5C), suggesting that the association between 2 and Ph₂DBTD is more favorable. Variable concentration experiments were performed for 2, RM, PhOH, and CO₂. These data show that the observed current density is proportional to the concentration of 2 (Figures S15 and S16), RM (Figures S17 and S18), a fixed ratio of 2 and RM (Figures S19 and S20), PhOH (Figures S21 and S22), and CO₂ (Figures S23 and S24) where RM is DBTD or Ph₂DBTD. The complexity of the overall co-catalytic system, with overlapping chemical and catalytic components, precludes us from making definitive rate dependence assignments from these data.

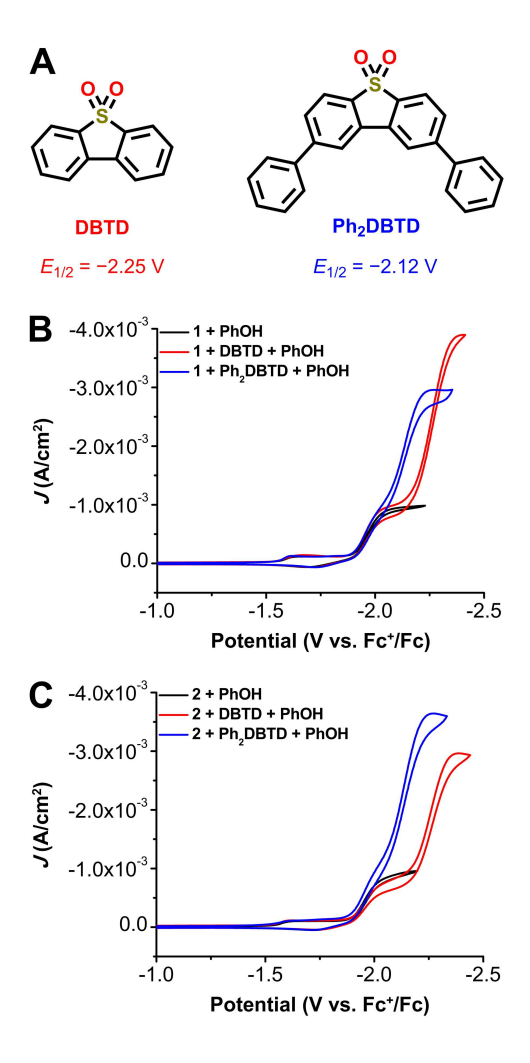


Figure 5. CVs of 1.0 mM Cr(^{tbu}dhbpy)Cl(H₂O) **1** (**A**) or Cr(^{tbu}dhphen)Cl(H₂O) **2** (**B**) in the absence (black) and presence of 2.5 mM DBTD (red) or Ph₂DBTD (blue) as the RM and 0.5 M PhOH under CO₂ saturation conditions. Conditions: 0.1 M TBAPF₆/DMF; glassy carbon working electrode, glassy carbon rod counter electrode, Ag/AgCl pseudoreference electrode; referenced to Fc⁺/Fc internal standard; 100 mV/s scan rate.

CPE experiments were performed to determine selectivity and activity of the coelectrocatalytic systems under protic conditions (**Figures S25** and **S26**). All CPE with the RMs were performed with a 1:5 ratio of catalyst:RM in order to compare to our previous systems.^{9, 11, 12} As has previously been the case, all systems remain quantitatively selective for the formation of CO with no H₂ production observed (**Tables S6** and **S7**; **Table 1**).^{9, 11, 12} Complexes **1**, **2**, and **3** show an increase in catalytic activity of one to two orders of magnitude when a RM is added to the system and all catalysts show the same relative trend in activity with the two RMs presented

here: Ph₂DBTD is the more active co-catalyst than DBTD (**Table 1**). While the trend is the same for both complex 1 and 2, there is a distinct difference in the relative increases when comparing systems. For the systems with 1, the TOF_{CPE} values are relatively similar to one another, despite the 130 mV difference in RM reduction potential. However, the TOF_{CPE} value more than doubles when switching the RM from DBTD to Ph₂DBTD with 2 as the catalyst (Table 1). This observed increase in activity with a decrease in the co-electrocatalytic overpotential conforms to the inverse potential scaling relationship we have observed previously. In this inverse scaling relationship, the favorability of mediator association to access a lower energy reaction pathway increases as the difference in redox potential between the two components decreases. The TOF_{CPE} values for the systems with 3 are still all higher than those for 2 due to the intrinsically higher activity of complex 3.9 However, the difference between the systems with 2 and 3 as the catalyst and Ph₂DBTD as the RM do not scale based on the difference in inherent catalyst activity, consistent with a difference in the extent of the RM interaction between catalysts, vide infra. Previous CPE controls with the RMs on their own showed non-quantifiable amounts of CO and significant H₂ produced under comparable conditions.^{9, 11, 12}

Table 1. Results of CPE experiments with PhOH under CO₂ saturation conditions.

Conditions	Potential (V vs Fc ⁺ /Fc)	FE _{CO} (%)	TOF_{CPE} (s^{-1})	η (V)	Turnovers of CO w.r.t [1 or 2]	Turnovers of CO w.r.t [RM]	$i_{ m cat}/i_{ m p}^{ m f}$
1 + PhOH ^{11, 12a}	-2.30	111±14	7.12	0.11	11.4	-	7.2
1 + DBTD + PhOH ^{11, 12b}	-2.30	102±14	65.3	0.41	29	5.8	4.6
$1 + Ph_2DBTD + PhOH^{9c}$	-2.20	100±2	69.3	0.28	22	5.3	4.8
$2 + PhOH^d$	-2.30	101±3	4.90	0.12	5.21	_	8.3
2 + DBTD + PhOH ^c	-2.30	94±7	56.3	0.41	13.7	2.7	3.4

$2 + Ph_2DBTD + PhOH^c$	-2.20	102±3	126	0.28	7.08	1.4	15
$3 + PhOH^{9e}$	-2.30	95±8	9.29	0.16	13	_	8.4
3 + DBTD + PhOH ^{9c}	-2.30	109±9	163	0.41	28	6.5	5.8
$3 + Ph_2DBTD + PhOH^{9c}$	-2.20	97±5	194	0.28	35	8.8	7.1

 $[^]a$ – 0.5 mM catalyst and 0.6 M PhOH; b – 0.5 mM catalyst, 2.5 mM RM, and 0.6 M PhOH; c – 0.1 mM catalyst, 0.5 mM RM, and 0.12 M PhOH; d – 0.5 mM catalyst and 1.0 M PhOH; e – 0.1 mM catalyst and 0.12 M PhOH; f – 1.0 mM catalyst and 0.5 M PhOH, scan rate = 100 mV/s.

We note that the observed CV current densities cannot be directly compared: while these current plateaus do directly relate to electrocatalytic activity, the diffusion-limited Faradaic current of the pre-catalyst system cannot be properly accounted for. In this case, the RMs do not interact with the Cr complexes in the absence of CO_2 , preventing a rigorous analytical comparison. However, an approximate accounting of this component can be achieved through a modified i_{cat}/i_p (i_{cat} = catalytic plateau current and i_p = Faradaic current) ratio where the co-electrocatalytic current becomes i_{cat} and the current of the RM is i_p , as previously described (**Table 1**; see the SI for details). The trend in the i_{cat}/i_p ratios is the same as the trend in TOF_{CPE} values for the respective co-catalytic systems of each complex.

Computational Studies

 active catalyst species is a four-coordinate complex formulated as $[Cr(^{tbu}dhbpy)]^-$ (generated from 1) or $[Cr(^{tbu}dhphen)]^-$ (generated from 2). A comparison of the CO_2 binding reaction to generate $[Cr(^{tbu}dhphen)(CO_2)]^-$ and $[Cr(^{tbu}dhbpy)(CO_2)]^-$ from these two species shows a minimal difference in the reaction barrier ($\Delta\Delta G^{\ddagger} = 0.3 \text{ kcal/mol}$), but it was found to be less endergonic ($\Delta\Delta G = -1.1 \text{ kcal/mol}$) for 2 (**Table 2**).

Table 2. Calculated activation and reaction free energies for CO₂ binding by [Cr(tbudhbpy)]⁻ and [Cr(tbudhphen)]⁻.

Cr Complex	ΔG^{\ddagger} Cr–CO ₂	ΔG Cr–CO ₂
	(kcal/mol)	(kcal/mol)
[Cr(tbudhbpy)(CO ₂)]	10.4	4.6
$[Cr(^{tbu}dhphen)(CO_2)]^-$	10.7	3.5

A comparison of the barrier for C–OH bond cleavage induced by protonation, which has previously been assessed to be the turnover frequency determining state (TDTS) for the bpy-based catalytic cycle, $^{31, 44}$ found that the barrier for the phen-based complex was again approximately isoergic with the bpy complex ($\Delta\Delta G^{\ddagger} = 0.2$ kcal/mol, **Table 3**). For both the bpy- and phen-based complex these species are proposed to be six-coordinate, with DMF bound to the axial position opposite to the [CO₂H]⁻ fragment. The equilibrium displacement of this axial DMF ligand by the reduced [RM]⁻, K_{RM} , was also evaluated. We have previously shown that the favorability of this equilibrium can dictate the extent to which the catalytic response reflects the faster co-catalytic cycle over the relatively slower intrinsic one. The free energies of formation of the proposed dianionic 4_0 Cr(CO₂H)(RM) $^{-2}$ assembly generated by the reaction described in Eq (1) for all known Cr-based systems are found in Table 3.

$${}_{1}^{3}\text{Cr}(\text{CO}_{2}\text{H})^{-1} + {}^{2}\text{RM}^{-1} \stackrel{K_{RM}}{\rightleftharpoons} {}_{0}^{4}\text{Cr}(\text{CO}_{2}\text{H})(\text{RM})^{-2} + \text{DMF}$$

Table 3. Calculated free energies of [RM]⁻ ligand displacement reaction summarized by Eq (1), calculated free energies of activation for the rate-limiting C-OH bond cleavage step and CO₂ binding. S = DMF, $[Cr(^{tbu}dhbpy)]^- = 1a$, $[Cr(^{tbu}dhphen)]^- = 2a$, and $[Cr(^{tbu}dh^{tbu}bpy)]^- = 3a$.

<u> </u>	[Sive all opj]	14, [01(ampinem)	zu, ana [er an	<u> </u>
	Cr Complex		$\Delta G \mathbf{Eq}$ (1) (kcal/mol)	ΔG^{\ddagger} C $-$ OH (kcal/mol)	Ref
	$[\mathbf{1a}(\mathrm{CO_2H})(\mathrm{S})]^-$		n/a	13.5	9
[$[\mathbf{1a}(\mathrm{CO_2H})(\mathrm{DBTD})]^{2-}$		-0.1	11.6	9
[1:	$a(CO_2H)(Ph_2DBTD)]^{2-}$		-3.1	11.6	9
	$[\mathbf{2a}(\mathrm{CO_2H})(\mathrm{S})]^-$		n/a	13.7	this work
[2a (CO ₂ H)(DBTD)] ²⁻		-1.8	10.4	this work
[2:	$a(CO_2H)(Ph_2DBTD)]^{2-}$		-5.6	11.9	this work
	$[\mathbf{3a}(\mathrm{CO_2H})\mathrm{S})]^-$		n/a	12.5	9
[$[\mathbf{3a}(\mathrm{CO_2H})(\mathrm{DBTD})]^{2-}$		-2.3	10.7	9
[3:	$a(CO_2H)(Ph_2DBTD)]^{2-}$		-6.1	10.8	9

Interestingly, although for the bpy-based system the displacement of DMF by [DBTD]⁻ is approximately isoergic ($\Delta G = -0.1 \text{ kcal/mol}$), the formation of the same adduct with the phen-based derivative is exoergic by -1.8 kcal/mol. This value is comparable to that which we have previously obtained for complex 3 of -2.3 kcal/mol at the same level of theory.⁹ This trend aligns with stronger interactions corresponding to closer energies of π^* systems, but we emphasize that greater dispersive interactions are also likely to contribute. The barrier for the proposed TDTS of the phen-based derivative of 10.4 kcal/mol is lower than that determined for the bpy-based of 11.6 kcal/mol. This barrier for the phen-based complex in the co-catalytic cycle again shows greater similarity with the barrier of 10.7 kcal/mol obtained for the more active catalyst, 3.9

The minimal difference in the barriers for CO_2 binding calculated for the phen- and bpy-based compounds implies an analogous electronic structure. Indeed, an assessment of the frontier KS orbitals and spin density of $[Cr(^{tbu}dhphen)]^-$ is consistent with the previous proposal of a S=3/2

ground state comprised of a Cr(II) center antiferromagnetically paired with a ligand-based radical anion (**Figure 6**).^{31, 44} Further, the distribution of added electron density in the ligands of $[Cr(^{tbu}dhphey)]^-$ and $[Cr(^{tbu}dhphen)]^-$ shows insignificant differences, despite the additional six-membered ring in the backbone of $[Cr(^{tbu}dhphen)]^-$. In the transition state for CO₂ binding, **TS**^{CO2}, a molecular orbital with significant π^* phen character contributes one of the two electrons necessary for the incipient Cr–CO₂ bond (**Figure S28**), analogous to what was found in computational studies on the bpy-based compound. Similar to the bpy-based compound, the bending of the CO₂ molecule in this transition state for the phen-based complex is asymmetric relative to the Cr–C bond vector, but only a single Cr–C σ bonding interaction is implied.

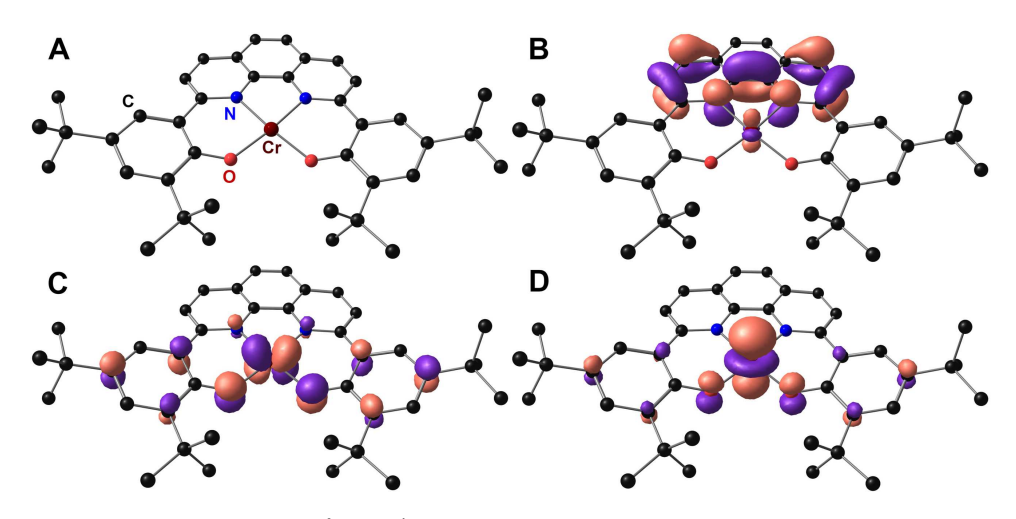


Figure 6. Molecular geometry of ${}_{0}^{4}$ **Cr**⁻¹ with H atoms omitted for clarity (**A**) Kohn-Sham orbital projection of SOMO (**B**), SOMO⁻¹ (**C**), and SOMO⁻² (**D**).

Unsurprisingly, the minor electronic structure differences found between the phen-based and bpy-based monoanionic active species and their respective transition states for CO_2 binding were also reflected in the respective TSs. Following protonation and reduction of the CO_2 adduct, association of the proton donor is expected to produce ${}_{1}^{3}Cr(CO_2H) \cdot (PhOH)^{-1}$, prior to C-OH bond cleavage. Analysis of the spin density and KS orbitals contributing to this interaction show that the redox activity of the phen-backbone again plays an analogous role to bpy in relaying an

electron to the Cr center, with only trivial differences in delocalization. Examination of \mathbf{TS}^{CO2H} shows transfer of electron density from the partially populated π^* orbital into the Cr center as proton transfer occurs.

The key differences between the phen- and bpy-based complexes appear to be primarily in the co-electrocatalytic cycle when Ph₂DBTD is included as the RM. In addition to the free energies of formation of the ${}^4_0\text{Cr(CO}_2\text{H)(RM)}^{-2}$ assembly, the quality of the pancake bonding interaction can be assessed by analyzing the vertical atom-atom overlap and distances between the ligand backbone and RM. PB is characterized as stronger than van der Waals interactions when the distances between the atoms are shorter and the vertical overlap between individual atoms is better, since orbital interactions can be maximized.²⁹ There is no clear difference in the atom-atom overlap between all of the assemblies with 1 and 2 as catalyst and DBTD and Ph₂DBTD as the RM (Figure 8 and Figures S39-S42). However, the centroid-centroid distances between the phen backbone of 2 and Ph₂DBTD are overall shorter (3.238, 3.200, 3.253 Å) than any of the other intermediates (Table S8), implying a relatively stronger contribution from PB to the favorable binding energy. Although in ${}^4_0\mathrm{Cr}(\mathrm{CO_2H})(\mathrm{DBTD})^{-2}$ both 1 and 2 have shorter distances between the central fivemembered rings, the centroid-centroid distances for the two six-membered rings are longer (Table **S8**). Since PB is also characterized by highly delocalized π electrons, increased distances for portions of the π -framework sharing the radical electron density will decrease the contribution of PB to the interaction energy. Since the electron delocalization and KS orbital composition in the phen and bpy fragments remains similar in the co-catalyst adducts, the data also imply that the relative contribution of dispersion interactions is increased for the phen backbone (2) relative to

the bpy (1): [DBTD]⁻ binding as summarized by **Eq (1)** is 1.7 kcal/mol more favorable than for the bpy analogue (1), which increases to be 2.5 kcal/mol more favorable for [Ph₂DBTD]⁻.

Proposed Mechanism

Based on these results, we can propose that complex 2 follows the same intrinsic and cocatalytic cycles as complexes 1 and 3 (Figure 7).^{7, 9, 11, 12, 31, 44} To initiate the intrinsic catalytic cycle, a four-coordinate neutral Cr species derived from complex 2 is reduced to a monoanionic four-coordinate species, i. This monoanionic species is best described as high-spin Cr(II) antiferromagnetically paired with a phen-centered radical anion, (phen⁻). This species then readily binds CO₂ to form [Cr–CO₂] ii which can then go on to be protonated by PhOH while binding DMF, before a favorable one-electron reduction generates [Cr–CO₂H]⁻ iii. Without a RM present (but at the potentials where the redox mediator is reduced), the catalyst can proceed via **Pathway** A, where protonation followed by reduction once again occurs to release H₂O and leave [Cr–CO]⁻ v. This intermediate is not stable and will readily release CO to form i and close the catalytic cycle. When a RM is present, the singly reduced [RM] will displace the DMF molecule in iii to give iv, ${}_{0}^{4}\mathrm{Cr(CO_{2}H)(RM)}^{-2}$ defined by K_{RM} as discussed above. This step allows for the reaction to proceed via **Pathway B**, where iv is protonated and water is released to give [Cr-CO] v. Since both catalysts are active for the reduction of CO₂ to CO with or without the presence of the RM at the tested conditions, it is reasonable to assume both Pathway A and Pathway B are being accessed at the same time. Therefore, the observed TOF values will represent a combination of catalytic and co-catalytic pathways.

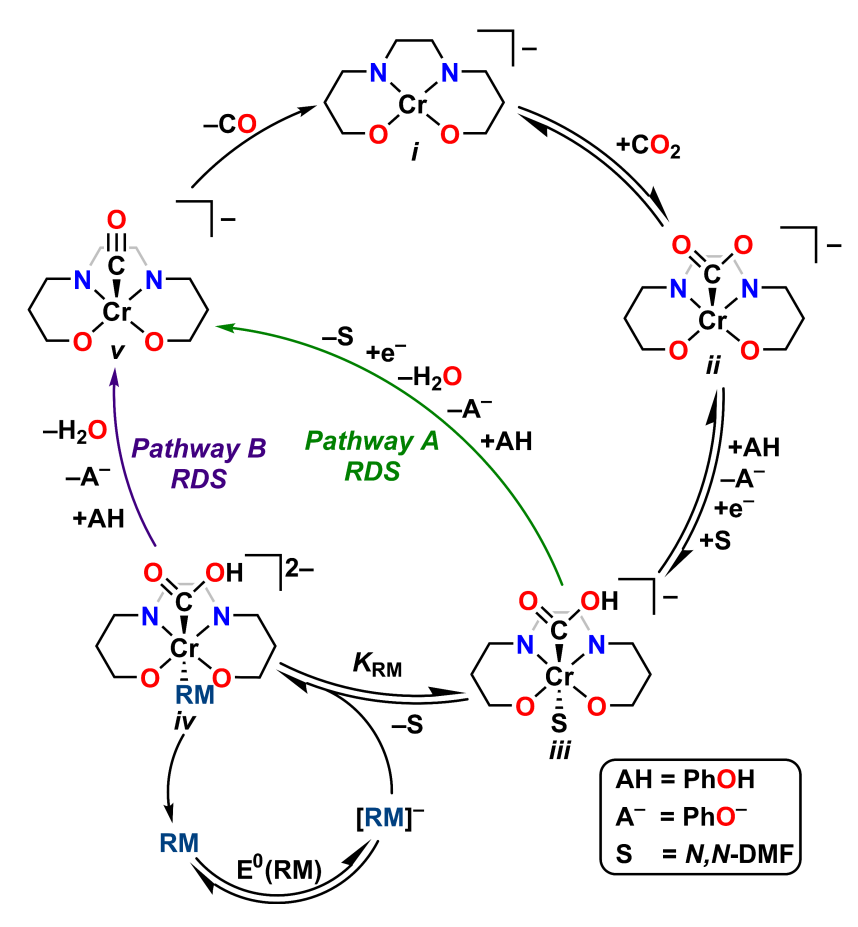


Figure 7. Proposed catalytic mechanism for electrocatalytic CO_2 reduction by Cr and coelectrocatalytic reduction of CO_2 by Cr and RM where Cr 1 or 2 and RM is DBTD or Ph_2DBTD . Initial reduction step to form i from catalyst as synthesized omitted for clarity.

Discussion

As was the case with 1 and 3 previously, 9 the experimental and computational results for 2 indicate an inner-sphere electron transfer mechanism under co-electrocatalytic conditions. In this mechanism, the reduced RM binds to the Cr center to give $_0^4$ Cr(CO₂H)(RM) $^{-2}$ prior to the rate-determining step, C–OH bond cleavage. Although the absolute TOF_{CPE} values determined for 1 with DBTD and PhOH present are approximately 10 s^{-1} faster than 2 under the same co-electrocatalytic conditions, the enhancements under co-catalytic conditions correspond to 9-fold and 11-fold increases from the intrinsic activities determined for these catalysts, respectively. In

other words, the co-catalytic enhancement for **2** is greater with DBTD than it is for **1**, consistent with the greater K_{RM} (1.7 kcal/mol more favorable ΔG).

The significant difference between 1 and 2 with Ph₂DBTD as the RM can likewise be rationalized using the difference in the thermodynamics of the equilibrium binding step in Eq 1. The difference in calculated ΔG Eq (1) values (Table 3) increases to favor 2 by 2.5 kcal/mol without a significant change in reaction barrier, suggesting that K_{RM} is one of the primary determinants in the observed increase in experimental TOF_{CPE} values (Table 1). As described above, increased binding favorability reflects both a greater contribution of the PB interaction to stabilizing the RM-bound intermediate ${}^4_0\text{Cr}(\text{CO}_2\text{H})(\text{RM})^{-2}$, as well as increased dispersion interactions. Here, two components are likely to contribute to the difference between 1 to 2: the slightly more negative reduction potential of 2, which better matches the RM reduction potential, and the increased aromatic character of the phen backbone, which should act to protect its radical character, as well as improve the magnitude of the PB and dispersion interactions. Since the computational data do not show significant delocalization of electron density into the additional six-membered ring of the phen backbone during key reaction steps, it is also clear that dispersion effects and steric protection are playing an increased role in stabilizing adduct formation.

Finally, we can compare the results described with complex 2 to those obtained with complex 3 (Figure 3C). The reduction potential of 3 is 40 mV closer to Ph₂DBTD than 2, but the activity only increases by a factor of 21 from the intrinsic response (ratio of catalytic and co-catalytic TOF values), in comparison to a factor of 26 for 2 (Table 1). Notably, the calculated structures of the ${}_{0}^{4}$ Cr(CO₂H)(RM) $^{-2}$ intermediate for 2 and 3 where RM is Ph₂DBTD show a clear steric hindrance effect on the binding interaction (Figure 8). In the structure with 2 as the

catalyst, there is very good vertical atom-atom overlap between the five and six member rings of Ph₂DBTD and the phen backbone, maximizing orbital interactions for the pancake bonding. For complex **3**, which has a di-*tert*-butyl-substituted bpy backbone, steric hindrance prevents an optimal interaction and causes Ph₂DBTD to be rotated to a position with poor vertical atom-atom overlap. This rotation and decrease in overlap will limit the strength of the PB interaction between **3** and Ph₂DBTD for purely steric reasons. However, the $\Delta\Delta G$ for Eq (1) favors the association of complex **3** by about 0.5 kcal/mol relative to complex **2** (Table 3). This suggests that any relative decrease in the quality of the PB based on steric clash is compensated to some degree by contributions from dispersion. Further, because of the more reducing Cr potential for **3**, the barrier for $\Delta\Delta G^{\ddagger}$ C-OH is favored by 1.1 kcal/mol with respect to **2** following the association of [Ph₂DBTD]⁻, which is reflected in the experimental observation of increased TOF_{CPE} for **3**. The relative uniformity of the ΔG^{\ddagger} C-OH barrier decrease upon RM association for all complexes – and its independence from the thermodynamics of Eq (1) – also indicates that the nature of Cr-sulfone bond formation in the axial position plays a key role.

However, the performance of **3** relative to **1** and **2** with Ph₂DBTD appears to be significantly *underperforming* in its potential co-electrocatalytic activity, which we propose is the consequence of the sterically controlled kinetic limitations on the association of the RM and Cr complex, prior to a formal bonding interaction. Interestingly, based on these data it also appears that PB and dispersion interactions have a compensatory relationship with respect to the favorability of Cr–RM adduct formation.

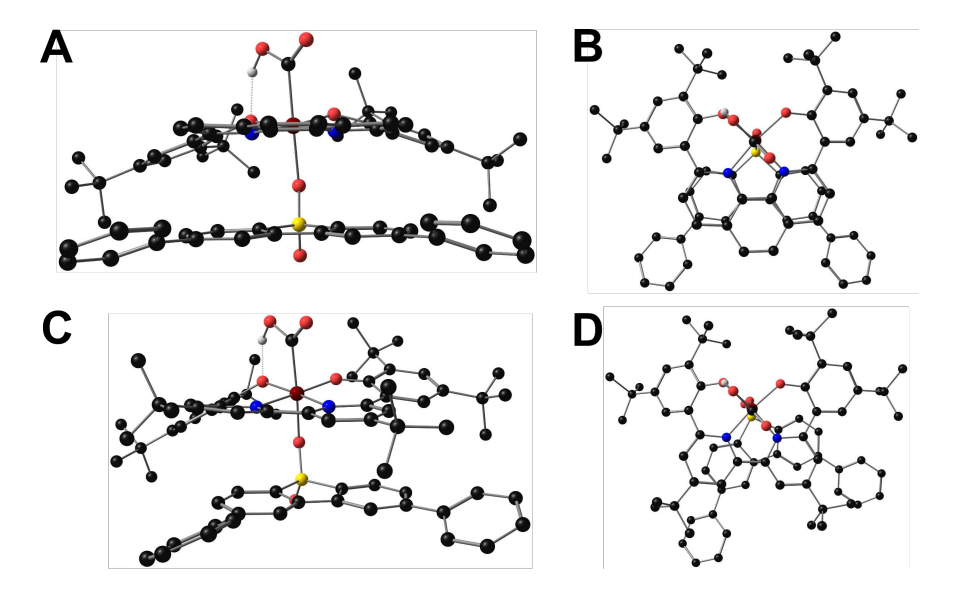


Figure 8. Molecular geometry of ${}^4_0\text{Cr}(\text{CO}_2\text{H})(\text{Ph}_2\text{DBTD})}^{-2}$ where Cr is the phen based complex **2** (**A** and **B**) or the *tert*-butyl substituted bpy complex **3** (**C** and **D**) with select H atoms removed for clarity.

Conclusion

Our previous reports demonstrate that increasing the PB interaction present in a key RM-bound intermediate by more closely matching the reduction potential of catalyst and RM can increase activity. However, the evidence presented here demonstrates that dispersion interactions can compensate for ideal orbital overlap between the π frameworks to some degree and that steric hindrance of the Cr-center also plays a significant role in controlling the rate of association between the RM and the Cr complex during co-electrocatalysis. Indeed, the increased aromatic character of the phen-backbone produces noteworthy co-catalytic enhancements, with a minimal change in catalyst reduction potential. In order to improve these systems in the future, these results indicate that we must identify catalysts and RMs that have closely matched reduction potentials and isolate new derivatives which maximize the planarity of the RM and catalyst backbone.

ASSOCIATED CONTENT

Supporting Information. Additional Material and Methods, CV, UV-vis, NMR, electrochemical data, and computational coordinates are included as supporting information. Crystal data has been deposited with the CCDC: 2221535-2221536.

AUTHOR INFORMATION

Corresponding Author. * - machan@virginia.edu

Funding Sources

University of Virginia.

Notes

The authors declare no competing financial interest.

ACKNOWLEDGMENT

This research was supported by the U.S. Department of Energy, Office of Science, Office of Basic Energy Sciences, Catalysis Science Program, under Award DE-SC0022219. Single crystal X-ray diffraction experiments were performed on a diffractometer at the University of Virginia funded by the NSF-MRI program (CHE-2018870). We acknowledge the University of Virginia for maintenance and support with the Rivanna High-Performance Computing Center.

References:

- 1. Carbon dioxide now more than 50% higher than pre-industrial levels https://www.noaa.gov/news-release/carbon-dioxide-now-more-than-50-higher-than-pre-industrial-levels.
- 2. De Luna, P.; Hahn, C.; Higgins, D.; Jaffer, S. A.; Jaramillo, T. F.; Sargent, E. H., What would it take for renewably powered electrosynthesis to displace petrochemical processes? *Science* **2019**, *364* (6438), eaav3506.
- 3. Azcarate, I.; Costentin, C.; Robert, M.; Saveant, J. M., Through-Space Charge Interaction Substituent Effects in Molecular Catalysis Leading to the Design of the Most Efficient Catalyst of CO₂-to-CO Electrochemical Conversion. *J. Am. Chem. Soc.* **2016**, *138* (51), 16639-16644.
- 4. Cometto, C.; Chen, L.; Lo, P.-K.; Guo, Z.; Lau, K.-C.; Anxolabéhère-Mallart, E.; Fave, C.; Lau, T.-C.; Robert, M., Highly Selective Molecular Catalysts for the CO₂-to-CO Electrochemical Conversion at Very Low Overpotential. Contrasting Fe vs Co Quaterpyridine Complexes upon Mechanistic Studies. *ACS Catal.* **2018**, 8 (4), 3411-3417.
- 5. Froehlich, J. D.; Kubiak, C. P., Homogeneous CO₂ Reduction by Ni(cyclam) at a Glassy Carbon Electrode. *Iorg. Chem.* **2012**, *51* (7), 3932-3934.
- 6. Sampson, M. D.; Nguyen, A. D.; Grice, K. A.; Moore, C. E.; Rheingold, A. L.; Kubiak, C. P., Manganese Catalysts with Bulky Bipyridine Ligands for the Electrocatalytic Reduction of Carbon Dioxide: Eliminating Dimerization and Altering Catalysis. *J. Am. Chem. Soc.* **2014**, *136* (14), 5460-5471.
- 7. Hooe, S. L.; Dressel, J. M.; Dickie, D. A.; Machan, C. W., Highly Efficient Electrocatalytic Reduction of CO₂ to CO by a Molecular Chromium Complex. *ACS Catal.* **2020**, *10* (2), 1146-1151.
- 8. Reid, A. G.; Hooe, S. L.; Moreno, J. J.; Dickie, D. A.; Machan, C. W., Homogeneous Electrocatalytic Reduction of CO₂ by a CrN₃O Complex: Electronic Coupling with a Redox-Active Terpyridine Fragment Favors Selectivity for CO. *Inorg. Chem.* **2022**, *61* (43), 16963-16970.
- 9. Reid, A. G.; Moreno, J. J.; Hooe, S. H.; Baugh, K. R.; Thomas, I. H.; Dickie, D. A.; Machan, C. W., Inverse Potential Scaling in Co-Electrocatalytic Activity for CO₂ Reduction Through Redox Mediator Tuning and Catalyst Design. *Chem. Sci.* **2022**, *13*, 9595-9606.
- 10. Reid, A. G.; Machan, C. W., Redox Mediators in Homogeneous Co-electrocatalysis. *J. Am. Chem. Soc.* **2023**, *145* (4), 2013-2027.
- 11. Hooe, S. L.; Moreno, J. J.; Reid, A. G.; Cook, E. N.; Machan, C. W., Mediated Inner-Sphere Electron Transfer Induces Homogeneous Reduction of CO₂ via Through-Space Electronic Conjugation**. *Angew. Chem., Int. Ed.* **2022**, *61* (1), e202109645.
- 12. Hooe, S. L.; Moreno, J. J.; Reid, A. G.; Cook, E. N.; Machan, C. W., Corrigendum: Mediated Inner-Sphere Electron Transfer Induces Homogeneous Reduction of CO₂ via Through-Space Electronic Conjugation. *Angew. Chem.*, *Int. Ed.* **2022**, *61* (25), e202205139.
- 13. Anson, C. W.; Stahl, S. S., Cooperative Electrocatalytic O₂ Reduction Involving Co(salophen) with p-Hydroquinone as an Electron-Proton Transfer Mediator. *J. Am. Chem. Soc.* **2017**, *139* (51), 18472-18475.
- 14. Badalyan, A.; Stahl, S. S., Cooperative electrocatalytic alcohol oxidation with electron-proton-transfer mediators. *Nature* **2016**, *535* (7612), 406-410.

- 15. Chalkley, M. J.; Del Castillo, T. J.; Matson, B. D.; Peters, J. C., Fe-Mediated Nitrogen Fixation with a Metallocene Mediator: Exploring pKa Effects and Demonstrating Electrocatalysis. J. Am. Chem. Soc. 2018, 140 (19), 6122-6129.
- 16. Galvin, C. M.; Waymouth, R. M., Electron-Rich Phenoxyl Mediators Improve Thermodynamic Performance of Electrocatalytic Alcohol Oxidation with an Iridium Pincer Complex. J. Am. Chem. Soc. **2020**, *142* (45), 19368-19378.
- 17. Garrido-Barros, P.; Derosa, J.; Chalkley, M. J.; Peters, J. C., Tandem electrocatalytic N₂ fixation via proton-coupled electron transfer. *Nature* **2022**, *609* (7925), 71-76.
- 18. Hooe, S. L.; Cook, E. N.; Reid, A. G.; Machan, C. W., Non-covalent assembly of proton donors and p-benzoquinone anions for co-electrocatalytic reduction of dioxygen. *Chem. Sci.* **2021**, *12*, 9733-9741.
- 19. McLoughlin, E. A.; Armstrong, K. C.; Waymouth, R. M., Electrochemically Regenerable Hydrogen Atom Acceptors: Mediators in Electrocatalytic Alcohol Oxidation Reactions. *ACS Catal.* **2020**, *10* (19), 11654-11662.
- 20. Smith, P. T.; Weng, S.; Chang, C. J., An NADH-Inspired Redox Mediator Strategy to Promote Second-Sphere Electron and Proton Transfer for Cooperative Electrochemical CO₂ Reduction Catalyzed by Iron Porphyrin. *Inorg. Chem.* **2020**, *59* (13), 9270-9278.
- 21. Dey, S.; Masero, F.; Brack, E.; Fontecave, M.; Mougel, V., Electrocatalytic metal hydride generation using CPET mediators. *Nature* **2022**, *607* (7919), 499-506.
- 22. Chambers, G. M.; Wiedner, E. S.; Bullock, R. M., H₂ Oxidation Electrocatalysis Enabled by Metal-to-Metal Hydrogen Atom Transfer: A Homolytic Approach to a Heterolytic Reaction. *Angew. Chem., Int. Ed.* **2018**, *57* (41), 13523-13527.
- 23. Gerken, J. B.; Stahl, S. S., High-Potential Electrocatalytic O₂ Reduction with Nitroxyl/NO_x Mediators: Implications for Fuel Cells and Aerobic Oxidation Catalysis. *ACS Cent. Sci.* **2015**, *1* (5), 234-243.
- 24. Alcázar-Fabra, M.; Navas, P.; Brea-Calvo, G., Coenzyme Q biosynthesis and its role in the respiratory chain structure. *Biochim. Biophys. Acta Bioenerg* **2016**, *1857* (8), 1073-1078.
- 25. Schneider, C. R.; Shafaat, H. S., An internal electron reservoir enhances catalytic CO₂ reduction by a semisynthetic enzyme. *ChemComm* **2016**, *52* (64), 9889-9892.
- 26. Johnson, D. C.; Dean, D. R.; Smith, A. D.; Johnson, M. K., STRUCTURE, FUNCTION, AND FORMATION OF BIOLOGICAL IRON-SULFUR CLUSTERS. *Annu. Rev. Biochem.* **2005**, *74*, 247-81.
- 27. Ibrahim, I. M.; Wu, H.; Ezhov, R.; Kayanja, G. E.; Zakharov, S. D.; Du, Y.; Tao, W. A.; Pushkar, Y.; Cramer, W. A.; Puthiyaveetil, S., An evolutionarily conserved iron-sulfur cluster underlies redox sensory function of the Chloroplast Sensor Kinase. *Commun. Biol.* **2020,** *3* (1), 13.
- 28. Chen, H.; Simoska, O.; Lim, K.; Grattieri, M.; Yuan, M.; Dong, F.; Lee, Y. S.; Beaver, K.; Weliwatte, S.; Gaffney, E. M.; Minteer, S. D., Fundamentals, Applications, and Future Directions of Bioelectrocatalysis. *Chem. Rev.* **2020**, *120* (23), 12903-12993.
- 29. Kertesz, M., Pancake Bonding: An Unusual Pi-Stacking Interaction. *Chem. Eur. J.* **2019**, *25* (2), 400-416.
- 30. Popowski, Y.; Moreno, J. J.; Nichols, A. W.; Hooe, S. L.; Bouchey, C. J.; Rath, N. P.; Machan, C. W.; Tolman, W. B., Mechanistic insight into initiation and regioselectivity in the copolymerization of epoxides and anhydrides by Al complexes. *Chem. Comm.* **2020**, *56* (90), 14027-14030.

- 31. Moreno, J. J.; Hooe, S. L.; Machan, C. W., DFT Study on the Electrocatalytic Reduction of CO₂ to CO by a Molecular Chromium Complex. *Inorg. Chem.* **2021**, *60* (6), 3635-3650.
- 32. Hooe, S. L.; Rheingold, A. L.; Machan, C. W., Electrocatalytic Reduction of Dioxygen to Hydrogen Peroxide by a Molecular Manganese Complex with a Bipyridine-Containing Schiff Base Ligand. *J. Am. Chem. Soc.* **2018**, *140* (9), 3232-3241.
- 33. Nichols, A. W.; Chatterjee, S.; Sabat, M.; Machan, C. W., Electrocatalytic Reduction of CO₂ to Formate by an Iron Schiff Base Complex. *Inorg. Chem.* **2018**, *57* (4), 2111-2121.
- 34. Hooe, S. L.; Machan, C. W., Dioxygen Reduction to Hydrogen Peroxide by a Molecular Mn Complex: Mechanistic Divergence between Homogeneous and Heterogeneous Reductants. *J. Am. Chem. Soc.* **2019**, *141* (10), 4379-4387.
- 35. Frisch, M. J.; Trucks, G. W.; Schlegel, H. B.; Scuseria, G. E.; Robb, M. A.; Cheeseman, J. R.; Scalmani, G.; Barone, V.; Petersson, G. A.; Nakatsuji, H.; Li, X.; Caricato, M.; Marenich, A. V.; Bloino, J.; Janesko, B. G.; Gomperts, R.; Mennucci, B.; Hratchian, H. P.; Ortiz, J. V.; Izmaylov, A. F.; Sonnenberg, J. L.; Williams; Ding, F.; Lipparini, F.; Egidi, F.; Goings, J.; Peng, B.; Petrone, A.; Henderson, T.; Ranasinghe, D.; Zakrzewski, V. G.; Gao, J.; Rega, N.; Zheng, G.; Liang, W.; Hada, M.; Ehara, M.; Toyota, K.; Fukuda, R.; Hasegawa, J.; Ishida, M.; Nakajima, T.; Honda, Y.; Kitao, O.; Nakai, H.; Vreven, T.; Throssell, K.; Montgomery Jr., J. A.; Peralta, J. E.; Ogliaro, F.; Bearpark, M. J.; Heyd, J. J.; Brothers, E. N.; Kudin, K. N.; Staroverov, V. N.; Keith, T. A.; Kobayashi, R.; Normand, J.; Raghavachari, K.; Rendell, A. P.; Burant, J. C.; Iyengar, S. S.; Tomasi, J.; Cossi, M.; Millam, J. M.; Klene, M.; Adamo, C.; Cammi, R.; Ochterski, J. W.; Martin, R. L.; Morokuma, K.; Farkas, O.; Foresman, J. B.; Fox, D. J. Gaussian 16 Rev. B.01, Wallingford, CT, 2016.
- 36. Becke, A. D., Density-functional thermochemistry. III. The role of exact exchange. *J. Chem. Phys.* **1993**, *98* (7), 5648-5652.
- 37. Lee, C.; Yang, W.; Parr, R. G., Development of the Colle-Salvetti correlation-energy formula into a functional of the electron density. *Phys. Rev. B* **1988**, *37* (2), 785-789.
- 38. Vosko, S. H.; Wilk, L.; Nusair, M., Accurate spin-dependent electron liquid correlation energies for local spin density calculations: a critical analysis. *Can. J. Phys.* **1980**, *58* (8), 1200-1211.
- 39. Stephens, P. J.; Devlin, F. J.; Chabalowski, C. F.; Frisch, M. J., Ab Initio Calculation of Vibrational Absorption and Circular Dichroism Spectra Using Density Functional Force Fields. *J. Phys. Chem.* **1994**, *98* (45), 11623-11627.
- 40. Weigend, F.; Ahlrichs, R., Balanced basis sets of split valence, triple zeta valence and quadruple zeta valence quality for H to Rn: Design and assessment of accuracy. *Phys. Chem. Chem. Phys.* **2005**, *7* (18), 3297-3305.
- 41. Weigend, F., Accurate Coulomb-fitting basis sets for H to Rn. *Phys. Chem. Chem. Phys.* **2006**, 8 (9), 1057-1065.
- 42. Grimme, S.; Antony, J.; Ehrlich, S.; Krieg, H., A consistent and accurate ab initio parametrization of density functional dispersion correction (DFT-D) for the 94 elements H-Pu. *J. Chem. Phys.* **2010**, *132* (15), 154104.
- 43. Grimme, S.; Ehrlich, S.; Goerigk, L., Effect of the damping function in dispersion corrected density functional theory. *J. Comput. Chem.* **2011**, *32* (7), 1456-1465.
- 44. Moreno, J. J.; Hooe, S. L.; Machan, C. W., Correction to DFT Study on the Electrocatalytic Reduction of CO2 to CO by a Molecular Chromium Complex. *Inorg. Chem.* **2022**.

TOC:

